metals

MDPI

Article

Microgalvanic Corrosion Behavior of Cu-Ag Active Braze Alloys Investigated with SKPFM

Armen Kvryan, Kari Livingston, Corey M. Efaw, Kyle Knori, Brian J. Jaques, Paul H. Davis, Darryl P. Butt and Michael F. Hurley *

Department of Materials Science and Engineering, College of Engineering, Boise State University, Boise, ID 83725-2090, USA; armenkvryan@boisestate.edu (A.K.); karilivingston@u.boisestate.edu (K.L.); coreyefaw@u.boisestate.edu (C.M.E.); kyleknori@u.boisestate.edu (K.K.); brianjaques@u.boisestate.edu (B.J.J.); pauldavis2@boisestate.edu (P.H.D.); darrylbutt@boisestate.edu (D.P.B.)

* Correspondence: mikehurley@boisestate.edu; Tel.: +1-208-426-4075

Academic Editors: Vineet V. Joshi and Alan Meier

Received: 3 February 2016; Accepted: 6 April 2016; Published: 19 April 2016

Abstract: The nature of microgalvanic couple driven corrosion of brazed joints was investigated. 316L stainless steel samples were joined using Cu-Ag-Ti and Cu-Ag-In-Ti braze alloys. Phase and elemental composition across each braze and parent metal interface was characterized and scanning Kelvin probe force microscopy (SKPFM) was used to map the Volta potential differences. Co-localization of SKPFM with Energy Dispersive Spectroscopy (EDS) measurements enabled spatially resolved correlation of potential differences with composition and subsequent galvanic corrosion behavior. Following exposure to the aggressive solution, corrosion damage morphology was characterized to determine the mode of attack and likely initiation areas. When exposed to 0.6 M NaCl, corrosion occurred at the braze-316L interface preceded by preferential dissolution of the Cu-rich phase within the braze alloy. Braze corrosion was driven by galvanic couples between the braze alloys and stainless steel as well as between different phases within the braze microstructure. Microgalvanic corrosion between phases of the braze alloys was investigated via SKPFM to determine how corrosion of the brazed joints developed.

Keywords: active braze alloy; corrosion; microgalvanic corrosion; electrochemistry; scanning kelvin probe force microscopy; stainless steel; Cu-Ag alloy; joining; scanning electron microscopy; energy dispersive spectroscopy

1. Introduction

Failure, whether chemical or mechanical in nature, often occurs where dissimilar materials are joined together. Common joining techniques range from mechanical fastening (e.g., bolt or rivet) to solid state joining (e.g., diffusion bonding). Brazing is an alternative joining technique in which a filler material is heated so as to form metallurgical bonds with the surfaces of the parts (parent materials) being joined. Brazing is a relatively low temperature process wherein the filler (braze material) is heated to a temperature above its melting point but below that of the parent materials. Joints formed by brazing can achieve very tight tolerances and offer desirable mechanical properties, similar to diffusion bonded materials, but have the advantage of being easily disassembled [1].

Many different braze alloys are available—designed for specific applications. A braze that performs well mechanically may have limited utility based on environmental compatibility. For example, silver-based braze alloys typically have a lower corrosion rate in an industrial atmosphere than in a marine environment [2]. When used in settings where contact with certain types of fuel may occur, silver-based brazes have poor corrosion resistance that can ultimately lead to failure [3]. The effect of brazing on the corrosion behavior of the resultant parts (including parent materials) has not

been widely investigated. Through gaining a better understanding of this vital relationship between brazing and its influence on corrosion behavior, it may be possible to optimize processing parameters and develop more effective brazes. Thus, it is important to understand the mechanism(s) that control the corrosion development at and near joints. Consequently, the impact of brazing on the corrosion behavior of the overall system is investigated in this work.

Background

The Cu-Ag based systems investigated in this study were chosen because of their ease of application, commercial availability, and favorable compatibility with common engineering metals and technical ceramics. Good materials compatibility is due in part to effective wetting. Wetting, the ability of a liquid to maintain contact with a solid surface, is an important factor in the overall effectiveness of a braze [4]. The wetting parameter, or wettability, is the geometric complement of the contact angle, and thus is inversely related to the contact angle [5]. During brazing, good compatibility is achieved when the braze alloy wets the target material well. This ensures excellent surface coverage and any diffusion that occurs does not result in poor mechanical behavior. To promote wetting and joint compliance, reactive elements are added to brazing alloys [1]. The resultant brazing alloys are known as active brazing alloys (ABA). Titanium is often added to silver based braze alloys in order to enhance their ability to wet the parent material(s) being joined, which is vital when joining dissimilar materials, including ceramics [1]. In addition, an increased amount of titanium in brazes has been found to yield thicker joints [6]. In this study, commercially available Cu-Ag-Ti and Cu-Ag-In-Ti braze alloys were obtained and used to join 316L stainless steel samples. It should be noted that oxide layers on stainless steel, including 316L, can act as a barrier to wetting, resulting in lower degrees of wettability for the braze [7]. The indium additions (~12%) present in the Cu-Ag-In-Ti braze lower the metal surface tension [8]. Additionally, indium additions in a titanium-containing braze alloy increase activity of titanium and wettability [8,9].

In any joining technique, the joint must preserve mechanical integrity and environmental compatibility. Heat input and the introduction of dissimilar materials may provide initiation spots for pitting corrosion at microstructural heterogeneities, galvanic attack at the metal/braze interface, or dealloying within the braze material. Initially, corrosion within the braze alloy may cause loss of joint integrity and sustained braze corrosion may create an aggressive local chemical environment that can lead to depassivation of the parent material. Relatively low temperature brazing alloys typically rely on noble metals to provide good wetting behavior, adhesion, and joint compatibility. However, these alloys generally provide a thermodynamic driving force for galvanic corrosion when joined with the parent metal and are exposed to conditions that support active corrosion. Galvanic corrosion as the mechanism of failure for silver based brazes coupled to stainless steels was first proposed by Takemoto *et al.* [10].

Current research on the effect of brazing has mainly focused on compatibility and resultant mechanical behavior [11–14]. However, once a candidate braze has been identified, the reliability and resistance to environmental attack must be addressed to determine long-term viability. With the exception of a few isolated studies [15–18], the effect of brazing on corrosion behavior has received little attention in the open literature [18]. Because of the multicomponent aspect of brazes, a multiphase microstructure is usually seen post brazing where the two parent materials are joined [18]. This is mainly due to precipitation of stable or meta-stable phases during the brazing cycle [16]. Once these phases are present, they would be expected to have different electrochemical behavior based on composition. The local potential difference between dissimilar regions in the microstructure will influence corrosion behavior, and is known as microgalvanic corrosion. The term microgalvanic corrosion describes a galvanic corrosion cell occurring on a sub-grain scale. Regions of varying composition result in potential differences amongst the individual phases in the braze, and tend to increase the corrosion rate of the less noble phases [16]. The concept of microgalvanic corrosion is

important to joint reliability, as manipulations of the filler metal in the braze can dramatically influence the overall corrosion behavior of a braze [19].

Confirmation of a microgalvanic corrosion mechanism requires accurate characterization of the surface of the materials, both in terms of composition and electrochemical potential. Scanning Kelvin Probe Force Microscopy (SKPFM) has been shown to be an effective technique to characterize expected electrochemical behavior of surface inhomogeneities within a metal alloy's microstructure [20]. A Kelvin probe measures the work function difference (Volta potential) between the surface of a sample and the probe itself. Correlation between the Volta potential difference (VPD) obtained via SKPFM and electrode solution potentials, and hence the likely development of galvanic couples during active corrosion conditions has previously been established [21]. However, this relationship should be approached with some caution for unconfirmed systems. SKPFM is a surface technique and sensitive to the formation of surface reaction products such as oxide layers that may influence the measurement, and thus may not always directly correlate with solution potential. However, by using an Atomic Force Microscope (AFM) with surface potential feedback and nullification, SKPFM is able to map Volta potential differences on a surface with extremely fine (sub-micron) resolution. Compared to other local techniques, SKPFM currently provides the highest achievable spatial resolution for studying corrosion initiation driven by microstructure inhomogeneities. This paper utilized SKPFM to analyze and characterize the VPD between the different metallic/intermetallic phases present within the brazes studied. This method was used to investigate and explain corrosion initiation and propagation driven by galvanic corrosion arising from compositional differences within brazing alloys used to join 316L stainless steel.

2. Materials and Methods

2.1. Materials and Joining Procedure

Commercial 316L stainless steel sheet with a thickness of 3 mm was water-jet cut into disk shaped samples of various sizes to be brazed. The braze alloys used were Cu-Ag-Ti-ABA with a thickness of approximately 50 μm and Cu-Ag-In-Ti-ABA with a thickness of 55 μm. Compositions of all materials are listed in Tables 1 and 2. Stainless steel disks were polished to a 1 μm finish with SiC polishing pads. The as-received Cu-Ag-Ti and Cu-Ag-In-Ti foils were lightly polished to an 800 grit finish and cut to sizes just smaller than the stainless steel disks. After polishing, all samples were ultrasonically cleaned in ethanol for 15 min, washed in deionized water, and dried using compressed air.

Table 1. Compositions in atomic percent of the braze alloys.

Material	Ag	Cu	Ti	In
Cu-Ag-Ti	63.1	35.1	1.8	–
Cu-Ag-In-Ti	59.00	27.25	1.25	12.5

Table 2. Compositions in atomic percent of the material being joined.

Material	C	P	Ni	Cr	Mn	Mo	N	Si	S	Fe
316L	0.0002	0.00036	0.101	0.1663	0.0168	0.0203	0.00066	0.00485	0.00026	Balance

Two geometrical configurations were used during brazing: sandwich (stainless steel/braze foil/stainless steel) and coated (braze foil on stainless steel disk). Prior to firing, the cleaned and polished samples were placed in an alumina boat wrapped in niobium foil and inserted into the furnace hot zone. The system was then purged with ultra-high purity argon gas (UHP Ar, 99.999%, Norco, Boise, ID, USA) for 20 min before continuously flowing with oxygen gettered UHP Ar. Stainless steel joining with Cu-Ag-Ti was achieved through the following thermal cycle suggested by the supplier: ramp to 700 °C (80 °C below the solidus temperature of Cu-Ag-Ti) at 5 °C/min and hold for 20 min

before ramping to 830 °C (15 °C above the liquidus temperature of Cu-Ag-Ti braze alloy) at a rate of 5 °C/min and held there for 15 min. The furnace was then cooled to room temperature at a rate of 5 °C/min. To create Cu-Ag-In-Ti joints, the furnace was ramped from room temperature to a temperature of 500 °C (130 °C below the solidus temperature of Cu-Ag-In-Ti) at a rate of 5 °C/min and held for 20 min, followed by a ramp to 730 °C (15 °C above the liquidus temperature of Cu-Ag-In-Ti) at a rate of 5 °C/min and held for 15 min, then cooled at a rate of 5 °C/min to room temperature, again as per the supplier recommendation.

2.2. Scanning Kelvin Probe Force Microscopy (SKPFM) of Brazed Regions

For SKPFM, brazed samples were cross sectioned, cold mounted in epoxy, and polished with progressively finer grit silicon carbide pads and diamond slurries starting with 400 grit and ending with a 1 μm diamond slurry. Next, the samples were cleaned ultrasonically in a bath of non-denatured (200 proof) High Performance Liquid Chromatography (HPLC)/spectrophotometric grade ethanol (Sigma-Aldrich, St. Louis, MO, USA). The final polishing step employed a VibroMet 2 vibratory polisher (Buehler, Lake Bluff, IL, USA) in which samples were polished for 1 h using a 12" Mastertex PSA pad (Buehler) covered with a 0.50 μm diamond slurry (MasterPrep Polishing Solution, Buehler). The polished samples were then rinsed with ethanol and blown dry with compressed air. Prior to imaging, an electrical connection between the sample surface and the AFM stage was established using colloidal silver paint and verified with a voltmeter. Imaging was conducted using a Bruker Dimension Icon AFM operating in frequency modulation Peak Force KPFM (FM PF-KPFM) mode with a PFQNE-AL probe (Bruker, Santa Barbara, CA, USA). PF-KPFM is a dual-pass method wherein the first pass acquires topography via Peak Force tapping (*i.e.*, rapid force curves). The second pass is then used to measure the tip-sample surface potential difference at a user-determined fixed lift height above the sample surface. The SKPFM technique and important experimental considerations have been described in greater detail previously [22], but lift heights of ~100 nm and a frequency modulation based detection scheme were employed. To enhance signal to noise and minimize the effects of residual sample roughness on the surface potential image, a slow scan rate was used (~0.05–0.1 Hz). Because SKPFM measures the difference in work function between the AFM probe and the sample surface (*i.e.*, the relative rather than absolute surface potential), potentials of the different phases are reported relative to each other. Absolute potentials can be determined; e.g., using an inert gold standard as a reference material.

2.3. Braze Phase Composition

A Scanning Electron Microscope (SEM) (Hitachi S-3400N-II, Hitachi, Tokyo, Japan) equipped with energy dispersive spectroscopy (EDS) capabilities was used to image and analyze the mounted braze joint cross-sections for both Cu-Ag-Ti and Cu-Ag-In-Ti alloys after SKPFM characterization. Performing SEM after SKPFM was to avoid effects of electron beam irradiation on the surface potential measured. The cross section of each braze alloy was imaged in both secondary electron mode and backscatter electron mode. Subsequently, elemental mapping was performed on the cross sections of each sample, along with multi-point analysis at selected locations.

2.4. Corrosion Testing

To assess corrosion behavior electrochemical and exposure testing in 0.6 M NaCl solution at room temperature (22–24 °C) was conducted. Potentiodynamic testing was performed on both the braze alloys and stainless steel samples separately following thermal treatment using the prescribed brazing furnace profile. The braze alloy samples were prepared by applying multiple coatings of either the foil or paste braze compound to one face of a stainless steel coupon. Multiple braze coatings ensured that only the braze material was exposed to solution when tested, with no impact from the underlying stainless steel possibly present at the pinholes that may occur with a single coating. A conventional

3-electrode cell with a Pt mesh counter electrode and a saturated calomel (SCE) reference electrode was used for potentiostat controlled polarization measurements.

3. Results

3.1. Brazed Stainless Steel Joint Characterization

Metallographic samples of the post-braze joint cross-section were examined via SEM in order to characterize the resulting joint (Figure 1). The joints formed a clean, tight, hermetic seal with the parent 316L samples. Both brazes were approximately 50 μm in width and displayed distinctive eutectic type phases in the braze region following the prescribed thermal cycles.

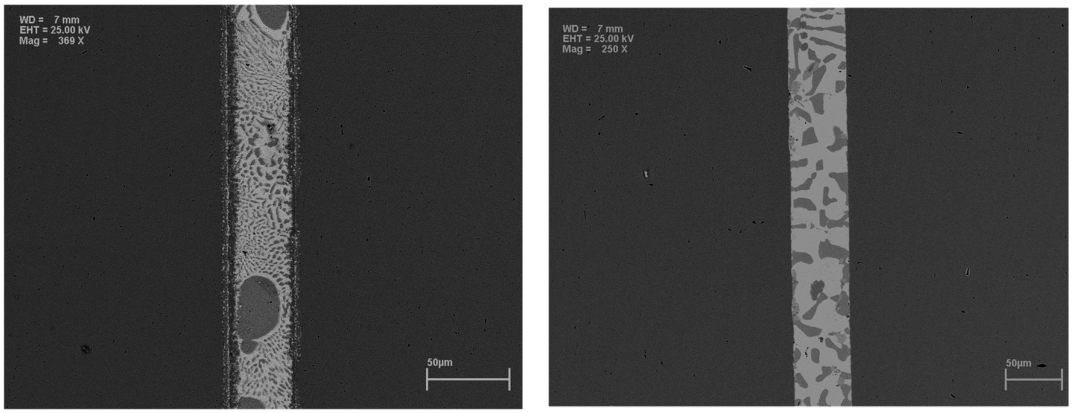

(**a**) (**b**)

Figure 1. Scanning Electron Microscopy (SEM) images of cross sections of the resultant braze joint between two stainless steel 316L samples joined using: Cu-Ag-Ti (**a**) and Cu-Ag-In-Ti (**b**) braze alloys.

EDS line scans are presented in Figure 2 (Cu-Ag-Ti) and Figure 3 (Cu-Ag-In-Ti) below. The Cu-Ag-Ti braze had a Ag-rich matrix with numerous distributed regions, generally ~1–10 μm across, of a precipitated Cu-rich phase. Generally, the EDS results did not indicate noticeable diffusion of the braze filler materials into the stainless steel. However, in a few areas the EDS scans indicated some transport of the braze alloy elements into the stainless steel, resulting in a Ti and Ag-containing region adjacent to the braze for the Cu-Ag-Ti braze sample. It was also observed that that the bulk of the titanium in the braze segregated to one side of the braze/stainless steel interface (Figure 2). The Cu-Ag-In-Ti braze phase structure consisted of an Ag-In-rich matrix phase with numerous regions of a precipitated Cu-rich phase. Ti was also found to be present in some of the Cu-rich regions.

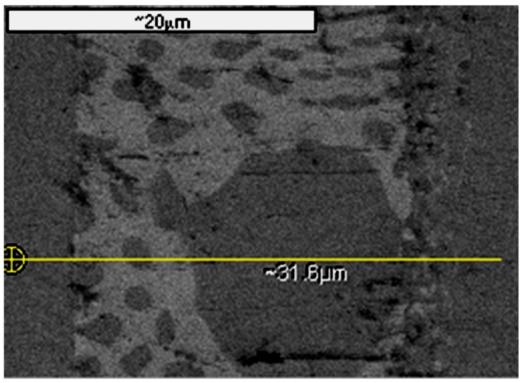

(**a**)

Figure 2. *Cont.*

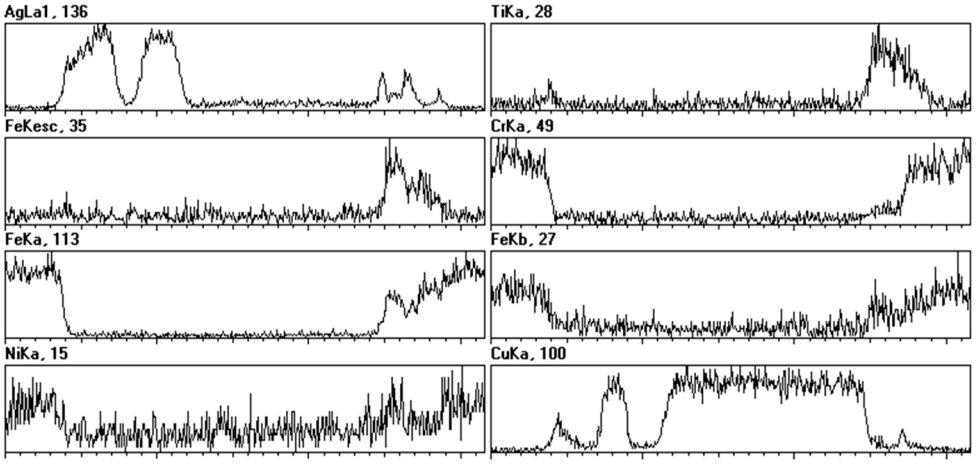

(**b**)

Figure 2. (**a**) SEM micrograph and (**b**) energy dispersive spectroscopy (EDS) line scan results from the cross section of a 316L stainless steel/Cu-Ag-Ti brazed joint.

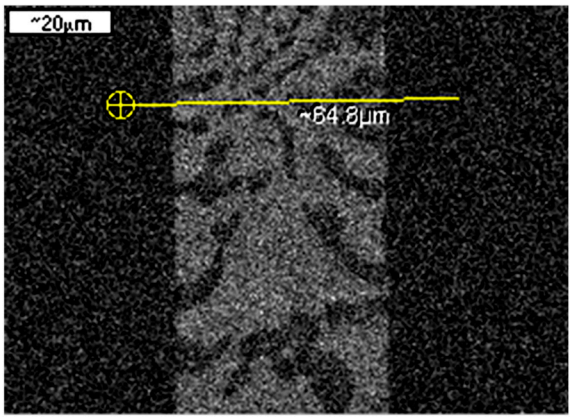

(**a**)

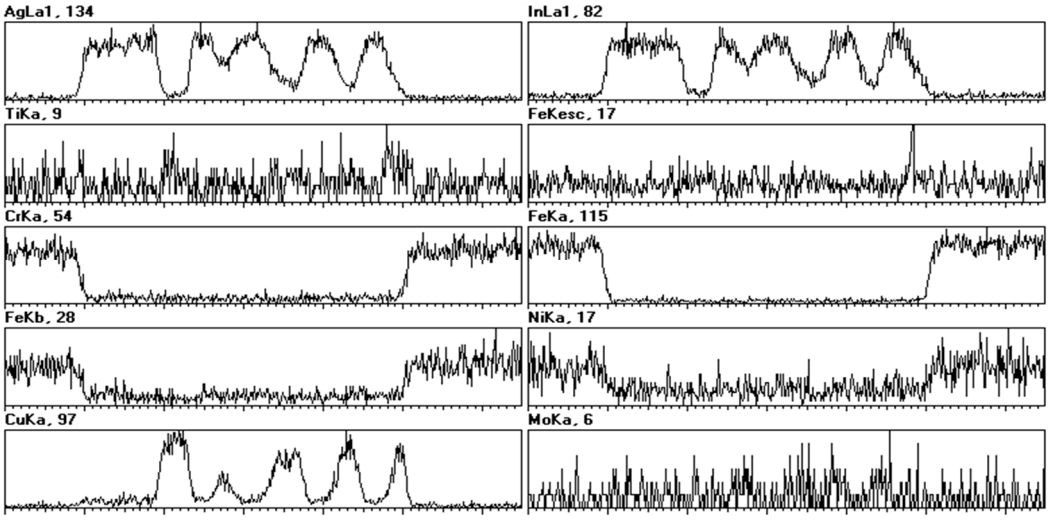

(**b**)

Figure 3. (**a**) SEM micrograph and (**b**) EDS line scans of a cross section of a 316L stainless steel/Cu-Ag-In-Ti brazed joint.

Phase separation within the braze regions was further characterized via optical microscopy to aid with identification of the various phases present when initiating SKPFM scans. Optical images obtained of the Cu-Ag-Ti and Cu-Ag-In-Ti braze areas showed clear variation of phase composition within the braze, with uniform 316L stainless steel on either side (Figure 4). The identical sample regions seen in Figure 4 were also characterized and discussed later in this paper.

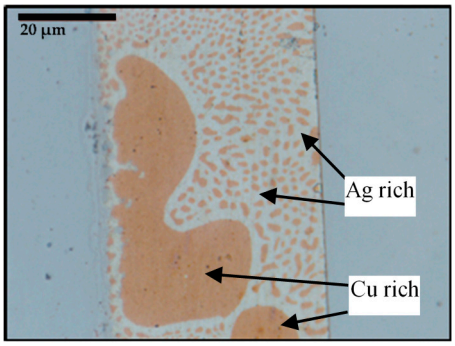

Phase	Cu	Ag	Ti
Cu Rich	94.65	5.10	0.50
Ag Rich	10.01	89.98	0.01

(**a**)

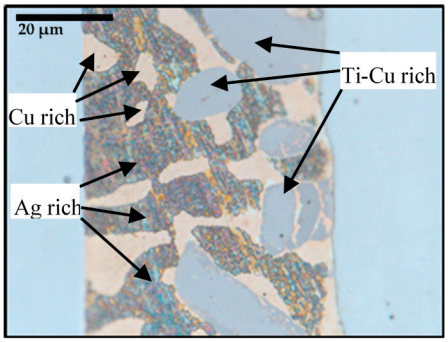

Phase	Cu	Ag	Ti	In
Cu Rich	90.18	5.86	2.09	1.88
Ag Rich	13.29	75.26	0	11.45
Cu-Ti Rich	77.27	0.84	21.21	0.67

(**b**)

Figure 4. Optical image of a Cu-Ag-Ti braze (**a**) and Cu-Ag-In-Ti braze (**b**) with labeled markers indicating the microconstituent phases present. Tables to the right of each image present average atomic % for each phase in (**a**) and (**b**), respectively, calculated from EDS data.

In order to obtain semi-quantitative compositions of the phases, EDS multi point scans were acquired for both Cu-Ag-Ti and Cu-Ag-In-Ti samples. Multiple spectra were taken at representative points within the individual phase regions of each sample. The average composition values in atomic percent obtained for each phase present are listed in the tables adjacent to the respective images (see Figure 4). The Cu-Ag-Ti sample had a standard deviation below 3, whilst the Cu-Ag-In-Ti had a standard deviation below 5.

For the Cu-Ag-Ti braze alloy, two primary phases, composed primarily of either copper or silver, dominate the microstructure of the braze in agreement with previous findings [8]. This bead-like microstructure develops with overall low solubility of titanium within the Cu-Ag-Ti braze. Titanium was not detected in the eutectic phases, but was instead found along the interface between the braze and parent stainless steel metal [8]. Additionally, some titanium diffused into the neighboring stainless steel. This was also observed in previous research, and is attributed to the lack of both titanium solubility within the braze and miscibility within the adjacent stainless steel, leading to near-complete segregation [8,23]. In contrast, three distinct phases were observed in the Cu-Ag-In-Ti brazed joint. Also, segregation of the titanium to the interface was suppressed. Ti content varied in and near regions where a distinct Cu-Ti phase was observed (Figure 4b) and suggested incomplete phase transformation. The Cu-Ti rich phase present was likely the Cu_4Ti intermetallic phase [23,24].

3.2. Corrosion Behavior of Brazed Joints

3.2.1. Electrochemical Testing of Braze Materials

Representative polarization curves from Cu-Ag-Ti (blue trace) and Cu-Ag-In-Ti (green trace) braze alloys are presented in Figure 5. Polarization data obtained from a bare 316L coupon (red trace) is also included in Figure 5 for comparison. The two different braze alloys displayed nearly identical polarization behavior. The braze alloys exhibited normal Tafel behavior indicative of activation polarization control with an corrosion rate, i_{corr} (at open circuit) of approximately 1×10^{-5} Amps/cm^2, approximately two orders of magnitude greater than the i_{corr} of passive 316L. Moreover, the E_{corr} (corrosion potential) of the braze alloys was approximately 50 mV less than that of 316L, −0.16 V *vs.* SCE.

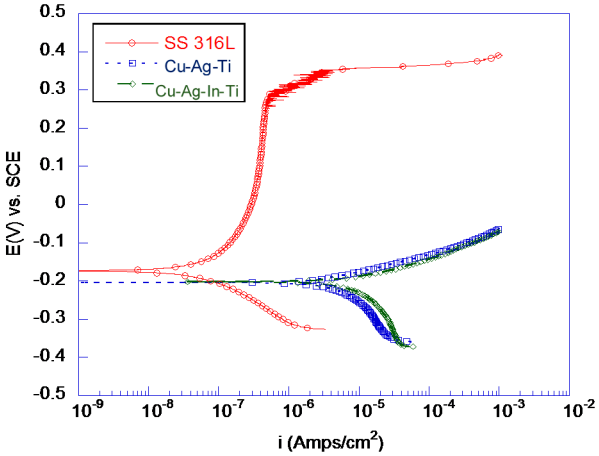

Figure 5. Potentiodynamic polarization scans conducted on brazes (blue and green traces) and a 316L stainless steel sample (red trace) in 0.6 M NaCl. The scan rate for all testing was 0.166 mV/s.

To determine any effect the thermal braze cycle might have on the inherent corrosion behavior of 316L, polarization curves were conducted on bare 316L samples that had been fired according to the braze cycle mentioned in the experimental section. When compared to the unfired stainless steel, the fired stainless steel sample displayed a much smaller passive region with pitting occurring at approximately 0.05 V *vs.* SCE (Figure 6). The pitting potential, or potential at which pitting corrosion occurs, was seen when a sharp increase in current occurred upon increasing potential. The pitting potential of the fired sample was significantly lower than the unfired 316L sample, likely due to grain boundary sensitization [25]. The effect on localized corrosion behavior could be expected since the sample was held in the sensitization range for approximately 35 min. Optical microscopy of the pitted surface (not shown here) revealed grain boundary attack had occurred at areas adjacent to pits on the fired sample. In contrast, pits on the unfired sample did not show evidence of preferential grain boundary attack near the pit openings, confirming some degree of sensitization on the 316L sample as a result of the thermal braze cycle.

3.2.2. Exposure Testing at Open Circuit Potential

Exposure testing was conducted to observe macroscopic corrosion propagation behavior of the braze alloy and stainless steel at the free corrosion potential under natural, galvanic coupling conditions. Circular braze foil coupons were fabricated such that the foil occupied approximately 80% of the exposed surface area of the polished face of the 316L disk. Following firing, the coated samples and an untreated 316L control sample were immersed in 0.6 M NaCl solution and the samples were observed periodically to monitor corrosion progression, as shown in Figure 7.

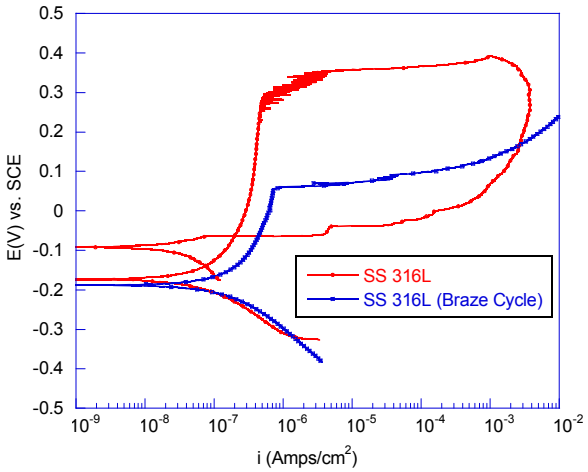

Figure 6. Potentiodynamic polarization scans conducted on 316L stainless steel subjected to a thermal brazing cycle (blue curve) compared to unfired 316L (red curve). Testing was conducted in 0.6 M NaCl with a scan rate 0.166 mV/s.

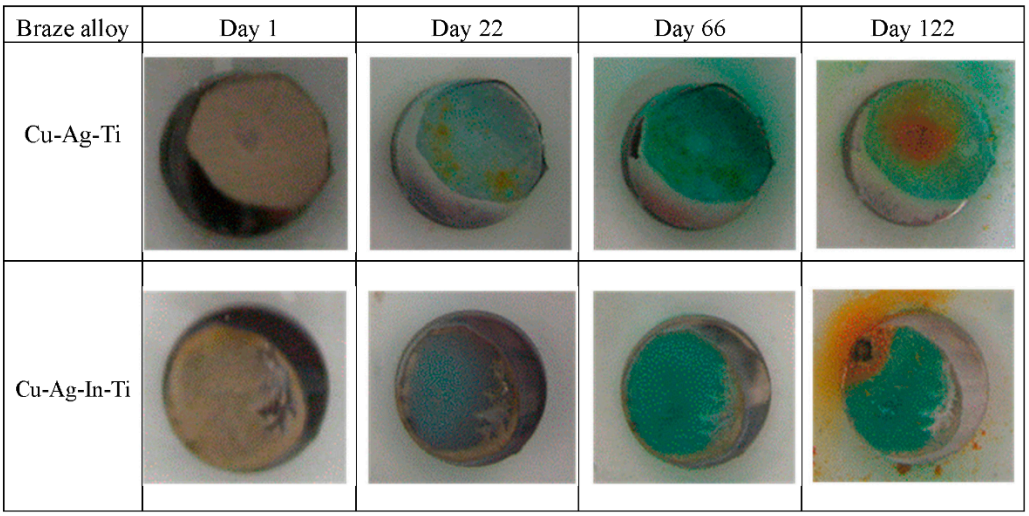

Figure 7. Time lapse photographs of corrosion propagation during long term exposure testing in 0.6 M NaCl. Cu-Ag-Ti (**top**) and Cu-Ag-In-Ti (**bottom**) braze alloy foil disks were used to coat ~80% of the exposed face area on 316L stainless steel samples. The stainless steel disk diameter was 16 mm for both samples.

The 316L control sample (not shown) did not display evidence of depassivation or production of any significant corrosion products for the duration of testing (166 days, or ~24 weeks). However, after only 22 days of immersion both of the braze foil coated samples showed evidence of macroscale corrosion damage (Figure 7). Visual observation revealed that corrosion was limited to the braze foil surface, while the remaining uncoated area of the 316L sample appeared unaffected. While the extent of the corrosion damage was not quantified, the presence of blue-green corrosion reaction products covering both the Cu-Ag-Ti and Cu-Ag-In-Ti foil surfaces suggested preferential corrosion of the Cu-rich phase present in each braze alloy [14]. Moreover, both samples also exhibited regions of dark red corrosion products deposited within the foil-coated region toward the end of the test duration. It is suspected these corrosion products were iron oxide-hydroxides generated from the underlying stainless steel which had become exposed following corrosion perforation of the braze foil coating.

3.3. SKPFM Measurements

SKPFM was used to measure Volta potential differences (VPD) among the various phases present on the surface of the brazed region of the stainless steel joint. SKPFM measurements were obtained prior to SEM/EDS characterization of the same regions on both braze alloy joints to avoid any effect of electron irradiation on surface potential measurements [22,26,27]. Potential maps acquired from SKPFM coupled with composition maps obtained from SEM/EDS clearly showed that the observed variations in potential correlated with changes in composition within the braze regions (Figures 8 and 9).

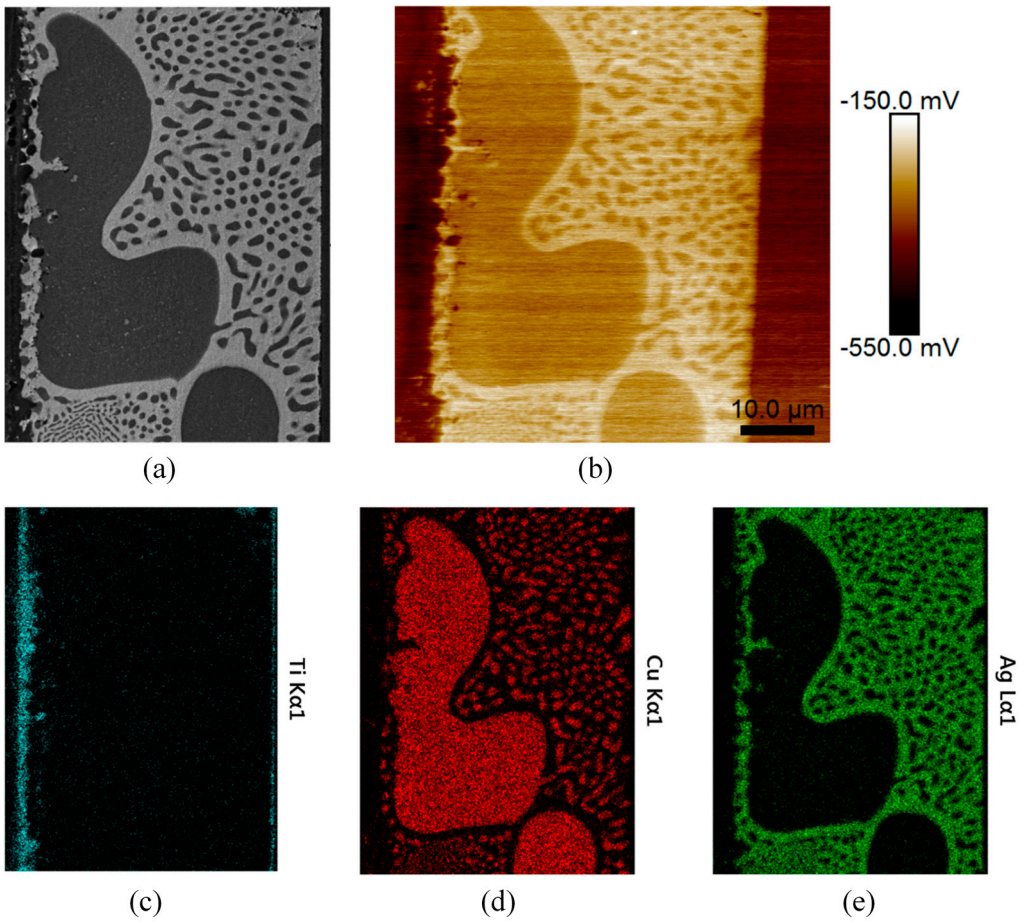

Figure 8. Secondary electron SEM image of Cu-Ag-Ti sample (**a**) followed by corresponding Scanning Kelvin Probe Force Microscopy (SKPFM) surface potential image (**b**). EDS elemental maps of the identical region for: Titanium (**c**); Copper (**d**); and Silver (**e**) are shown.

From the SKPFM VPD data, there is a clear difference in potential values between the two primary phases for the Cu-Ag-Ti braze sample, with the Ag-rich phase as the brighter or more noble area, and the Cu-rich phase darker (more active potential). The Volta potential observed for the stainless steel outside the braze region was more negative than either of the braze phases (Figure 8b). These differences are expected based solely on composition, and the difference promotes dissimilar metal, galvanic couple driven corrosion within the braze alloy. Similar results were obtained on the Cu-Ag-In-Ti sample, with the most noble phase being the Ag-rich phase. The most active braze phase is the Cu-Ti rich phase, while the Volta potential of the Cu-rich phase falls in between the two. The surrounding stainless steel was similar to the Ti-Cu rich phase (Figure 9).

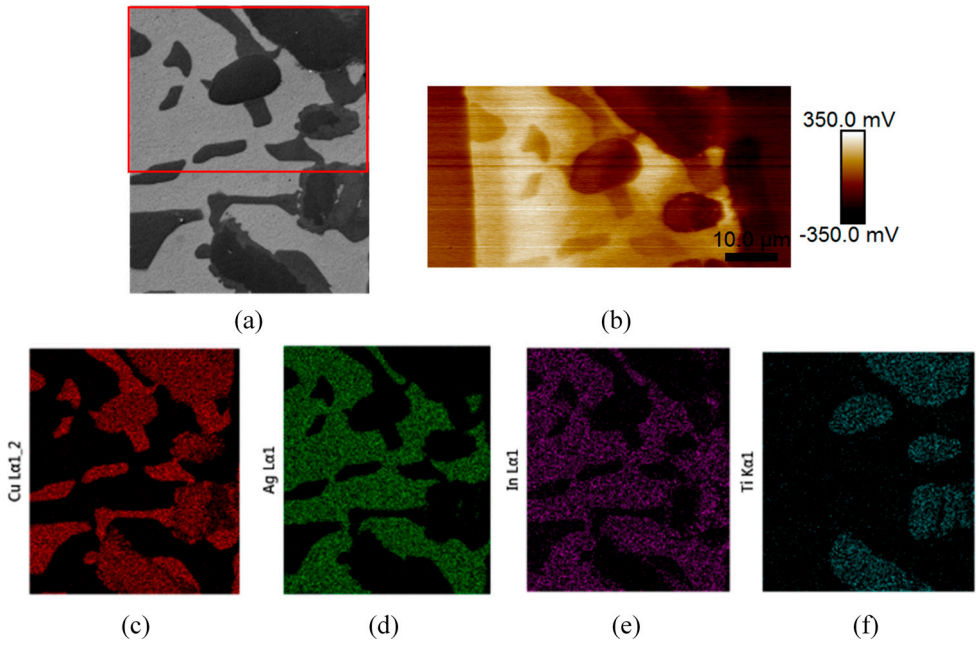

Figure 9. Secondary electron SEM image of Cu-Ag-In-Ti sample with the red box indicating where SKPFM was performed (**a**). SKPFM surface potential image (**b**) and EDS elemental maps of the identical region for: Copper (**c**); Silver (**d**); Indium (**e**); and Titanium (**f**) are shown.

4. Discussion

Research on braze reliability has largely focused on evaluating mechanical integrity of the joint [11–14]. Accordingly, corrosion behavior of brazes has received little attention in the open literature. The limited studies available focusing on stainless steel have considered different Ag-based braze compositions than studied here, but the systems behaved similarly and it was proposed that galvanic cells developed at the braze-stainless steel interface promoting corrosion driven by the electrically connected dissimilar metals [10,15–18,28]. However, in these studies, local galvanic couple corrosion was only postulated from bulk corrosion observations, it was not directly confirmed as in the present work with SKPFM. Other studies observed that partitioning of more noble alloying elements (preferred cathode sites) within the braze alloy occurred, causing depletion in the surrounding matrix and likely lead to preferential corrosion in those regions. In the systems investigated herein, similar corrosion behavior was confirmed [15–17]. Visual observation of corrosion propagation on braze alloy-stainless steel couples (Figure 7) showed that active corrosion rapidly initiated on the braze alloy first, with the surrounding uncoated stainless steel unaffected. The polarization curves presented in Figure 5 also suggest that the more anodic braze alloy will be preferentially attacked at an increased corrosion rate when galvanically connected to the more noble stainless steel cathode. Stainless steel had an open circuit potential (OCP) approximately 50 mV more noble that either of the braze alloys alone. On a macroscale, the stainless steel acts as cathode when galvanically coupled to the more anodic braze alloys, driving preferential corrosion of the braze alloy. This galvanic couple situation is particularly detrimental for joint integrity because of the typically large cathode (stainless steel) to anode (braze alloy) area ratio. At free corrosion conditions the anodic reaction occurring on the braze alloy is polarized towards the stainless steel, further accelerating the anodic reaction rate of the braze alloy. Because of the large cathode to anode area ratio there is ample cathode area available to support the increased dissolution rate of the braze, leading to eventual loss of joint integrity.

Following initiation, during corrosion propagation, the stainless steel also becomes susceptible to corrosion degradation near the braze interface, which is a further detriment to joint integrity. Corrosion attack on a 316L coupon with a foil braze coating on the surface showed that the copper phase was

preferentially attacked, and the presence of the braze alloy served as a crevice former under which localized corrosion was able to propagate into the stainless steel (Figure 10). In Figure 10, the samples were exposed for 7 days to 0.6 M NaCl at OCP followed by a potentiodynamic scan from open circuit to 0.5 V *vs.* SCE, prior to cleaning and cross sectioning. The left image (Figure 10) was obtained from a cross section that bisected a corrosion pit which grew and propagated underneath the braze alloy coating. Eventual corrosion attack of the stainless steel in a brazed sample was also observed during free corrosion conditions when immersed in 0.6 M NaCl solution. As seen in Figure 7, the generation of voluminous dark red corrosion products indicated that braze alloy corrosion likely generated a sufficiently aggressive local chemical environment to depassivate the underlying stainless steel. While the uncoated regions of the stainless steel coupon did not display evidence of corrosion damage, it is evident that the galvanically driven braze alloy corrosion led to subsequent corrosion attack of the joined stainless steel at the interface for both braze alloys considered.

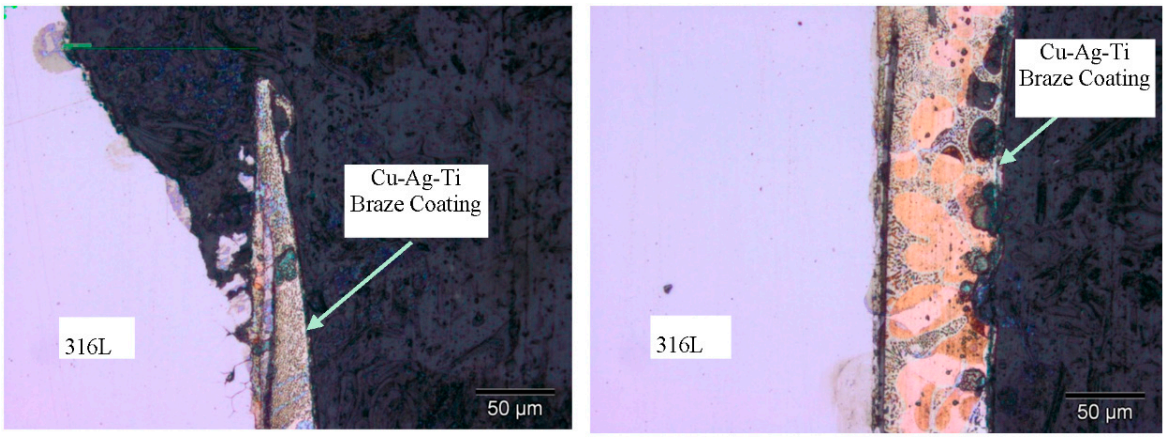

Figure 10. Cross sectioned 316L stainless steel sample with a Cu-Ag-Ti braze alloy coating following exposure for seven days in 0.6 M NaCl followed by a potentiodynamic scan.

For the Cu-Ag-Ti braze alloy, corrosion caused by segregation of Ti to the braze-stainless steel interface (Figure 8) could also promote loss of joint coherency. The image on the right in Figure 10 shows preferential corrosion attack on the Cu-rich phase of the braze alloy and an area of corrosion damage along the 316L and Cu-Ag-Ti coating interface. The behavior of Ti was similar to that observed in literature [2] and can be attributed to the strong interfacial reactions between the Cu and Ti found in the braze [5]. The addition of In in the Cu-Ag-In-Ti samples did not support Ti segregation to the joint interface, and hence would be expected to be beneficial to joint integrity.

In addition to the macroscale galvanic couple between braze alloys and stainless steel, both braze alloys formed multiple distinct phases following thermal treatment, resulting in microgalvanic cells between phases during active corrosion conditions. Open circuit potentials obtained from potentiodynamic polarization testing of both braze alloys were intermediate to those listed in the galvanic series for seawater for pure copper and pure silver [15,29]. Based on the galvanic series, the measured OCP of the bulk two phase (copper-rich and silver-rich) braze structure is in agreement with what would be expected from mixed potential theory. Within the braze alloy the expected electrode potential difference implies that when corrosion occurs, the Cu-rich phase of the braze alloy will be anodic to the more noble Ag-rich phase and suffer from preferential microgalvanic attack, even in the absence of a stainless steel couple.

The nature of microgalvanic corrosion within the braze alloys was further investigated with SKPFM. The goal of using SKPFM was to measure Volta potential differences between phases within the microstructure to determine relative nobility of the individual phases. Schmutz and Frankel, along with Leblanc, have established a direct correlation between Volta potentials measured in air and respective solution potentials of metals [26,27,30]. Importantly, the VPD observed was an effective indicator of how corrosion developed due to microstructural features. Subsequent to these findings, several research groups [31–39] have been able to verify that SKPFM is both reliable and effective in characterizing various alloy systems to accurately explain corrosion initiation behavior.

Galvanic corrosion on the microscale strongly influenced corrosion within the braze alloys. As determined via SKPFM, within the Cu-Ag-Ti braze, the Ag-rich phase was the most noble, followed by the Cu-rich phase, and finally stainless steel had the lowest overall potential (see Figure 11a, Table 3). For the Cu-Ag-In-Ti braze, the Ag-rich phase is the most noble, followed by the Cu-rich phase, then the Ti-Cu rich phase, as in Figure 12a,b and Table 4. The approximate average Volta potentials differences between phases in both braze alloys are presented in Tables 3 and 4 with corresponding images of the SKPFM images of the brazes in Figures 11 and 12 respectively. The SKPFM data presented in Figures 11 and 12 are from identical areas characterized with SEM/EDS (Figures 8 and 9). The co-localization of SKPFM and SEM/EDS techniques at the identical area provides direct evidence of the influence of local composition on Volta potential. Hence, in addition to the galvanic couple between the braze and stainless steel, variations in composition between phases provided the basis for microgalvanic corrosion within the braze alloys studied.

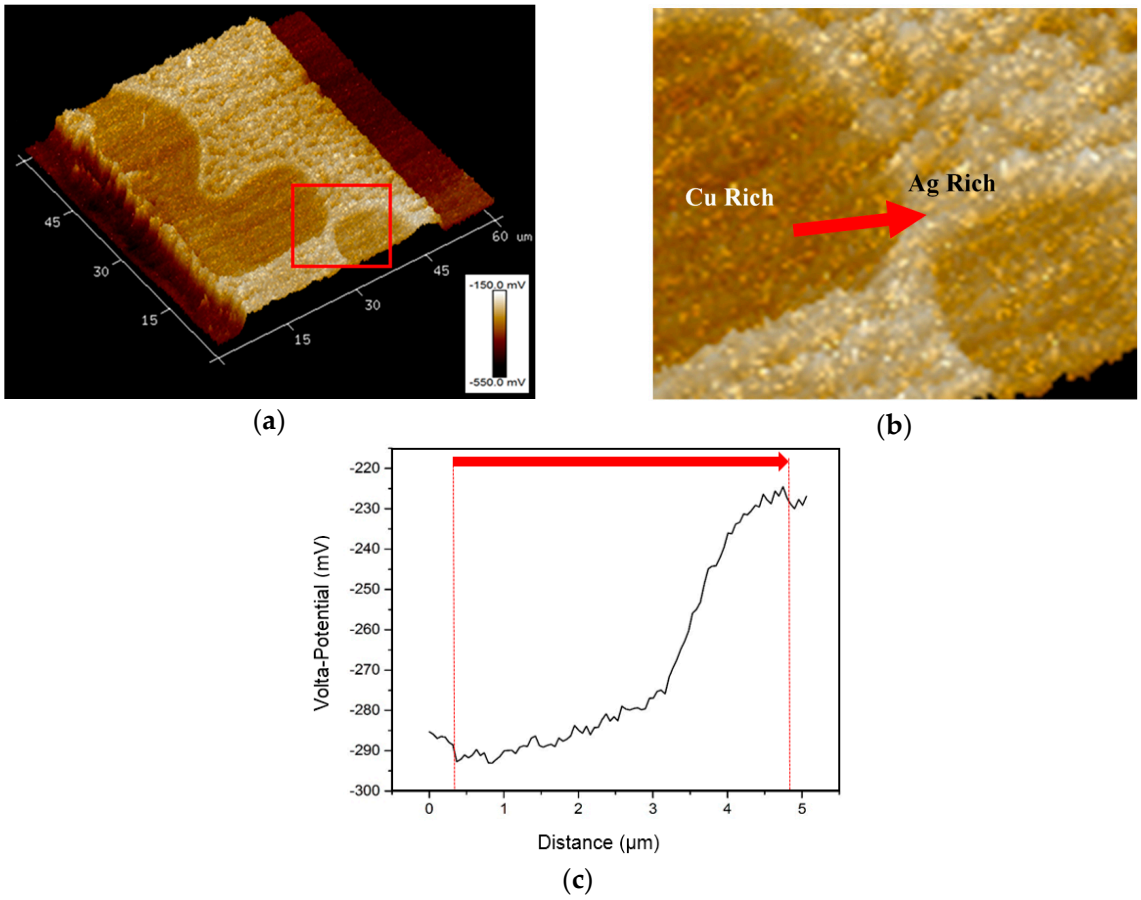

Figure 11. (**a**) Three dimensional (3-D) SKPFM Volta potential image of Cu-Ag-Ti sample with a box indicating area of scan; (**b**) Zoomed in image with arrow indicating where scan was taken; and (**c**) Graph of potential values obtained from scan as a function of distance with indicating arrow.

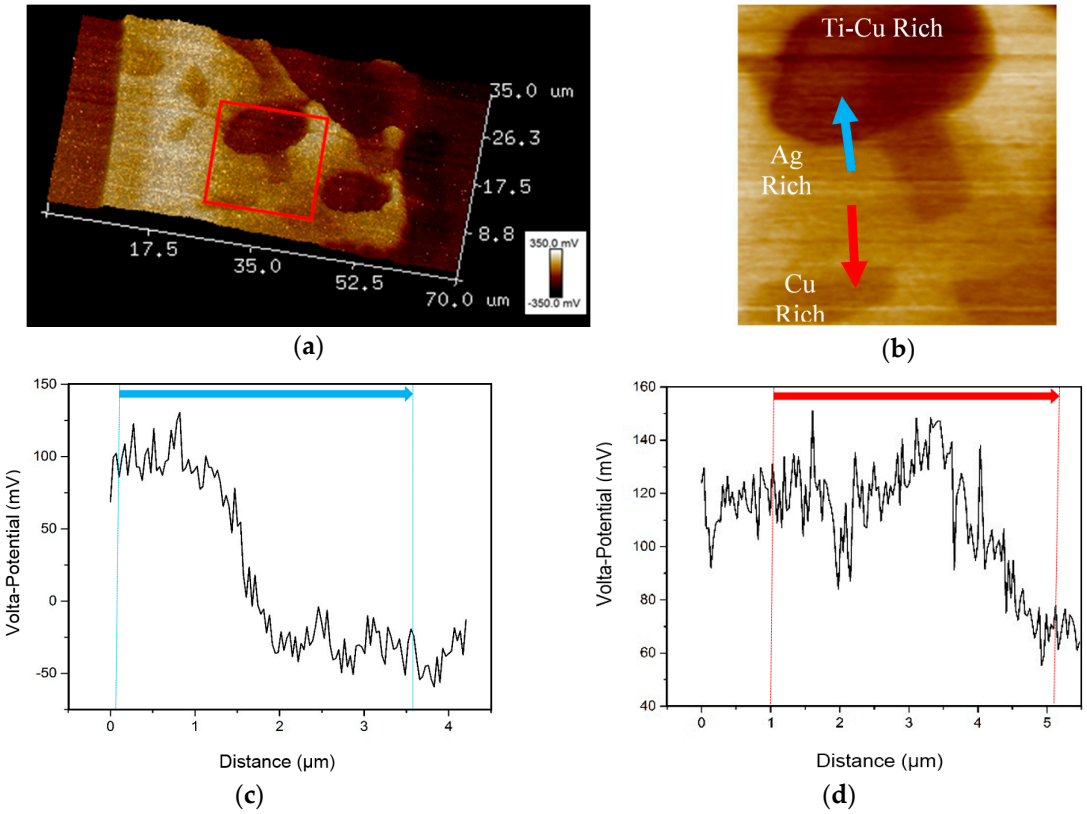

Figure 12. (**a**) 3-D SKPFM potential image of Cu-Ag-In-Ti sample with a box indicating area of scan. (**b**) Zoomed in image with arrows indicating where scan was taken. Graph of potential values obtained from scan as a function of distance with indicating arrow: (**c**) Blue arrow (Ag-rich phase to Ti-Cu-rich phase); and (**d**) Red arrow (Ag-rich phase to Cu-rich phase).

Table 3. Relative Volta potential difference (VPD) values in mV of phases within the Cu-Ag-Ti brazed joint. The first phase/metal is the more positive of the two.

Microgalvanic Couple (Cathode–Anode)	ΔVPD (±30 mV)
Ag Rich–Cu Rich	59
Cu Rich–Stainless steel	94

Table 4. Relative VPD in mV of the Cu-Ag-In-Ti sample. The first phase/metal is the more positive of the two.

Microgalvanic Couple (Cathode–Anode)	ΔVPD (±30 mV)
Ag Rich–Cu Rich	52
Cu Rich–(Ti-Cu) Rich	97
(Ti-Cu) Rich–Stainless Steel	53

Interestingly, SKPFM results showed the stainless steel surface had an average Volta potential that was less noble than any of the braze phases measured (Figures 11 and 12). This is contrary to the known and observed corrosion behavior, in that corrosion preferentially occurs within the braze alloy, with the coupled stainless steel acting as a cathode in the galvanic couple (Figures 5 and 7). *This finding is important because it highlights an instance where caution must be exercised when inferring electrochemical behavior from Volta potential measurements*. In the case of stainless steel, the presence of a protective passive oxide layer makes it an ineffective anode, and the resulting solution potential is more noble

than the braze material. Hence, it is essential to verify expected relative nobility obtained from SKPFM measurements with the observed corrosion and electrochemical behavior in solution, as done here.

5. Conclusions

The composition, phase separation, surface potential differences, and corrosion behavior of Cu-Ag braze alloys (Cu-Ag-Ti and Cu-Ag-In-Ti) and the joined material (316L) were investigated and correlated. SKPFM measurements provided new insight to the origins of microgalvanic corrosion within the brazed region and confirmed the manner that corrosion develops, which previously had only been postulated to explain bulk corrosion observations of brazed joints. Significant findings include:

(1) Co-localized SKPFM and SEM/EDS provided evidence of phase separation within the braze regions that resulted in surface potential differences. Moreover, the measured surface potentials correlated with the observed microgalvanic corrosion behavior, thereby highlighting the utility of combining these methods for the future study, prediction, and prevention of microgalvanic corrosion.

(2) Microgalvanic cells were confirmed via SKPFM VPD values. The two phases present in the Cu-Ag-Ti braze alloy samples differed by ~60 mV in surface potential, while the Cu-Ag-In-Ti samples exhibited a range in surface potential differences up to ~250 mV across three phases.

(3) Electrochemical testing on the individual materials was used to verify expected galvanic behavior. Stainless steel exhibited passive behavior and had an OCP that was noble to either of the braze alloys, which exhibited active corrosion behavior and i_{corr} approximately two orders of magnitude larger than stainless steel. The role of stainless steel in the direction of the galvanic couple was in conflict with that expected from SKPFM measurements and provided an exceptional case where SKPFM Volta potential did not correlate with solution potential.

(4) Exposure testing of stainless steel samples coated with each braze alloy were conducted at OCP in 0.6 M NaCl. It was found the braze alloy undergoes active corrosion that induces accelerated attack on the underlying 316L material. Additionally, it was seen that the Cu-rich phase of the braze alloy underwent preferential attack compared to the Ag-rich phase and corrosion propagation in the braze alloy was aggressive enough to depassivate the adjacent 316L stainless steel.

(5) The thermal brazing cycle caused sensitization of the 316L parent material and resulted in grain boundary attack and a pitting potential that was approximately 200 mV more negative than the unfired 316L.

Acknowledgments: Fabrication of samples was supported by National Science Foundation contract no. OISE-0709664. The generous support of the Boise State Surface Science Laboratory (SSL), the Center for Advanced Energy Studies (CAES), and Central Metallurgical Research & Development Institute, Egypt are also acknowledged. The authors thank Jasen B. Nielsen for assistance with SKPFM sample preparation.

Author Contributions: Michael F. Hurley, Paul H. Davis and Darryl P. Butt conceived and designed the experiments; Corey M. Efaw, Armen Kvryan and Michael F. Hurley performed the experiments; Kari Livingston, Armen Kvryan, Paul H. Davis and Corey M. Efaw analyzed the data; Kyle Knori, Brian J. Jaques, Darryl P. Butt and Paul H. Davis contributed reagents, materials and analysis tools. All authors contributed to writing the paper.

Conflicts of Interest: The authors declare no conflict of interest.

References

1. Jacobson, D.M.; Humpston, G. *Principles of Brazing*; ASM International: Materials Park, NY, USA, 2005.
2. Dev, S.C.; Singh, I.; Basu, D.K.; Bhattamishra, A.K.; Sivaramakrishnan, C.S. Corrosion behaviour of silver brazing alloys in different environments. *Anti-Corros. Methods Mater.* **1997**, *44*, 260–264. [CrossRef]
3. Dimatteo, A.; Lovicu, G.F.; Desanctis, M.; Valentini, R.; Santarelli, S.; Cognetta, F. Compatibility of nickel and silver-based brazing alloys with E85 fuel blends. *Mater. Corros.* **2015**, *66*, 158–168. [CrossRef]
4. Shafrin, E.G.; Zisman, W.A. Constitutive relations in the wetting of low energy surfaces and the theory of the retraction method of preparing monolayers. *J. Phys. Chem.* **1960**, *64*, 519–524. [CrossRef]
5. Dezellus, O.; Eustathopoulos, N. Fundamental issues of reactive wetting by liquid metals. *J. Mater. Sci.* **2010**, *45*, 4256–4264. [CrossRef]

6. Paiva, O.C.; Barbosa, M.A. Microstructure, mechanical properties and chemical degradation of brazed AISI 316 stainless steel/alumina systems. *Mater. Sci. Eng.* **2008**, *480*, 306–315. [CrossRef]
7. Kozlova, O.; Voytovych, R.; Devismes, M.F.; Eustathopoulos, N. Wetting and brazing of stainless steels by copper-silver eutectic. *Mater. Sci. Eng.* **2008**, *495*, 96–101. [CrossRef]
8. Abed, A.; Jalham, I.S.; Hendry, A. Wetting and reaction between β′-sialon, stainless steel and Cu-Ag brazing alloys containing Ti. *J. Eur. Ceram. Soc.* **2001**, *21*, 283–290. [CrossRef]
9. Nicholas, M.G.; Valentine, T.M.; Waite, M.J. The wetting of alumina by copper alloyed with titanium and other elements. *J. Mater. Sci.* **1980**, *15*, 2197–2206. [CrossRef]
10. Takemoto, T.; Okamoto, I. Effect of composition on the corrosion behavior of stainless-steels brazed with silver-base filler metals. *Weld. J.* **1984**, *63*, S300–S307.
11. Lee, J.G.; Hong, S.J.; Lee, M.K.; Rhee, C.K. High strength bonding of titanium to stainless steel using an Ag interlayer. *J. Nucl. Mater.* **2009**, *395*, 145–149. [CrossRef]
12. Liu, C.C.; Ou, C.L.; Shiue, R.K. The microstructural observation and wettability study of brazing Ti-6Al-4V and 304 stainless steel using three braze alloys. *J. Mater. Sci.* **2002**, *37*, 2225–2235. [CrossRef]
13. Singh, M.; Shpargel, T.P.; Asthana, R. Brazing of stainless steel to yttria-stabilized zirconia using gold-based brazes for solid oxide fuel cell applications. *Int. J. Appl. Ceram. Technol.* **2007**, *4*, 119–133. [CrossRef]
14. Singh, M.; Shpargel, T.P.; Asthana, R. Brazing of yttria-stabilized zirconia (YSZ) to stainless steel using Cu, Ag, and Ti-based brazes. *J. Mater. Sci.* **2008**, *43*, 23–32. [CrossRef]
15. Anastasio, S.; James, J.; Fitz-Gerald, J.; Scullly, J.R. Corrosion of superaustenitic stainless steel N08367 brazed with a nickel-chromium-silicon-phosphorous alloy: Electrochemical corrosion behavior of isolated and combined materials. *Corrosion* **2009**, *65*, 388–403. [CrossRef]
16. James, J.P.; Bocher, F.; Scully, J.R. Effect of braze clearance on localized corrosion of a superaustenitic stainless steel brazed with a Ni-based alloy (Ni-22Cr-6.3Si-3.8P). *Corrosion* **2009**, *65*, 511–526. [CrossRef]
17. Sorensen, N.R. The environmentally assisted failure of cusil in mattssons solution. *Corrosion* **1986**, *42*, 299–306. [CrossRef]
18. Lee, M.K.; Park, J.J.; Lee, J.G.; Rhee, C.K. Phase-dependent corrosion of titanium-to-stainless steel joints brazed by Ag-Cu eutectic alloy filler and Ag interlayer. *J. Nucl. Mater.* **2013**, *439*, 168–173. [CrossRef]
19. Chiu, L.H.; Wu, C.H.; Chang, H. Galvanic corrosion on vacuum-brazed UNS S31803 duplex stainless steel using Ni-Cr-Fe-P alloy filler metals. *Corrosion* **2007**, *63*, 127–134. [CrossRef]
20. Guillaumin, V.; Schmutz, P.; Frankel, G.S. Characterization of corrosion interfaces by the scanning kelvin probe force microscopy technique. *Electrochem. Soc.* **2001**, *148*, 163–173. [CrossRef]
21. Schmutz, P.; Frankel, G.S. Corrosion study of AA2024-T3 by scanning kelvin probe force microscopy and *in situ* atomic force microscopy scratching. *J. Electrochem. Soc.* **1998**, *145*, 2295–2306. [CrossRef]
22. Hurley, M.F.; Efaw, C.M.; Davis, P.H.; Croteau, J.R.; Graugnard, E.; Birbilis, N. Volta potentials measured by scanning kelvin probe force microscopy as relevant to corrosion of magnesium alloys. *Corrosion* **2015**, *71*, 160–170. [CrossRef]
23. Yue, X.; He, P.; Feng, J.C.; Zhang, J.H.; Zhu, F.Q. Microstructure and interfacial reactions of vacuum brazing titanium alloy to stainless steel using an agcuti filler metal. *MTL Mater. Charact.* **2008**, *59*, 1721–1727. [CrossRef]
24. Elrefaey, A.; Tillmann, W. Effect of brazing parameters on microstructure and mechanical properties of titanium joints. *J. Mater. Process. Technol.* **2009**, *209*, 4842–4849. [CrossRef]
25. Jones, D. *Principles and Prevention of Corrosion*, 2nd ed.; Prentice Hall: Upper Saddle River, NJ, USA, 1996.
26. Schmutz, P.; Frankel, G.S. Characterization of AA2024-T3 by scanning kelvin probe force microscopy. *J. Electrochem. Soc.* **1998**, *145*, 2285–2295. [CrossRef]
27. Schmutz, P.; Frankel, G.S. Influence of dichromate ions on corrosion of pure aluminum and AA2024-T3 in NaCl solution studied by AFM scratching. *J. Electrochem. Soc.* **1999**, *146*, 4461–4472. [CrossRef]
28. Chiu, L.H.; Hsieh, W.C.; Ling, Y.C. Effect of vacuum brazing on corrosion resistance of UNS S31803 and UNS S31200 duplex stainless steels. *Corrosion* **2002**, *58*, 797–803. [CrossRef]
29. Forman, C.M.; Verchot, E.A. *Practical Galvanic Series*; Report No. RS-TR-67-11; Army Missile Command: Redstone Arsenal, AL, USA, 1967.
30. Leblanc, P.; Frankel, G.S. A study of corrosion and pitting initiation of AA2024-T3 using atomic force microscopy. *J. Electrochem. Soc.* **2002**, *149*, B239–B247. [CrossRef]

31. Jia, J.X.; Atrens, A.; Song, G.; Muster, T.H. Simulation of galvanic corrosion of magnesium coupled to a steel fastener in NaCl solution. *Mater. Corros.* **2005**, *56*, 468–474. [CrossRef]
32. De Wit, J.H.W. Local potential measurements with the SKPFM on aluminium alloys. *Electrochim. Acta* **2004**, *49*, 2841–2850. [CrossRef]
33. Campestrini, P.; van Westing, E.P.M.; van Rooijen, H.W.; de Wit, J.H.W. Relation between microstructural aspects of AA2024 and its corrosion behaviour investigated using AFM scanning potential technique. *Corros. Sci.* **2000**, *42*, 1853–1861. [CrossRef]
34. Lacroix, L.; Ressier, L.; Blanc, C.; Mankowski, G. Combination of AFM, SKPFM, and SIMS to study the corrosion behavior of S-phase particles in AA2024-T351. *J. Electrochem. Soc.* **2008**, *155*, C131–C137. [CrossRef]
35. Femenia, M.; Canalias, C.; Pan, J.; Leygraf, C. Scanning kelvin probe force microscopy and magnetic force microscopy for characterization of duplex stainless steels. *J. Electrochem. Soc.* **2003**, *150*, B274–B281. [CrossRef]
36. Sathirachinda, N.; Pettersson, R.; Pan, J.S. Depletion effects at phase boundaries in 2205 duplex stainless steel characterized with SKPFM and TEM/EDS. *Corros. Sci.* **2009**, *51*, 1850–1860. [CrossRef]
37. Sathirachinda, N.; Pettersson, R.; Wessman, S.; Kivisakk, U.; Pan, J.S. Scanning kelvin probe force microscopy study of chromium nitrides in 2507 super duplex stainless steel-implications and limitations. *Electrochim. Acta* **2011**, *56*, 1792–1798. [CrossRef]
38. Mato, S.; Alcala, G.; Woodcock, T.G.; Gebert, A.; Eckert, J.; Schultz, L. Corrosion behaviour of a Ti-base nanostructure-dendrite composite. *Electrochim. Acta* **2005**, *50*, 2461–2467. [CrossRef]
39. Afshar, F.N.; de Wit, J.H.W.; Terryn, H.; Mol, J.M.C. Scanning kelvin probe force microscopy as a means of predicting the electrochemical characteristics of the surface of a modified AA4XXX/AA3XXX (Al alloys) brazing sheet. *Electrochim. Acta* **2013**, *88*, 330–339. [CrossRef]